Chemical Science

ROYAL SOCIETY OF CHEMISTRY

EDGE ARTICLE

View Article Online
View Journal | View Issue

Open Access Article. Published on 20 July 2022. Downloaded on 4/2/2026 10:18:28 AM.
This article is licensed under a Creative Commons Attribution-NonCommercial 3.0 Unported Licence.

Check for updates

Cite this: *Chem. Sci.*, 2022, **13**, 9401

All publication charges for this article have been paid for by the Royal Society of Chemistry

Crystal engineering of ferrocene-based charge-transfer complexes for NIR-II photothermal therapy and ferroptosis†

Wei Ge,[a] Chao Liu,[a] Yatao Xu,[a] Jiayao Zhang,[a] Weili Si,[*a] Wenjun Wang,[b] Changjin Ou*[c] and Xiaochen Dong[*ad]

Received 10th June 2022
Accepted 19th July 2022

DOI: 10.1039/d2sc03273b

rsc.li/chemical-science

Organic charge-transfer complexes (CTCs) can function as versatile second near-infrared (NIR-II) theranostic platforms to tackle complicated solid tumors, while the structure–property relationship is still an unanswered problem. To uncover the effect of molecular stacking modes on photophysical and biochemical properties, herein, five ferrocene derivatives were synthesized as electron donors and co-assembled with electron-deficient F4TCNQ to form the corresponding CTCs. The crystalline and photophysical results showed that only herringbone-aligned CTCs (named anion-radical salts, ARS NPs) possess good NIR-II absorption ability and a photothermal effect for short π–π distances (<3.24 Å) and strong π-electron delocalization in the 1D F4TCNQ anion chain. More importantly, the ARS NPs simultaneously possess ·OH generation and thiol (Cys, GSH) depletion abilities to perturb cellular redox homeostasis for ROS/LPO accumulation and enhanced ferroptosis. *In vitro* experiments, FcNEt-F4 NPs, and typical ARS NPs, show outstanding antitumor efficiency for the synergistic effect of NIR-II photothermal therapy and ferroptosis, which provides a new paradigm to develop versatile CTCs for anti-tumor application.

Introduction

Organic charge-transfer complexes (CTCs), composed of a well-aligned electron donor (D) and acceptor (A), often possess unique physical properties distinguished from the parent molecules, including conductibility, paramagnetism, thermoelectricity, and luminescence.[1–3] These fascinating characteristics of CTCs come from their new electronic structure and aggregation state which make them ideal functional materials for optoelectronic devices.[4,5] Besides, recent advances have demonstrated that CTCs show strong near-infrared (NIR) light-harvesting ability and a good photothermal effect due to the intense charge transfer interaction and activation of non-radiative pathways, which make CTCs one kind of promising NIR-absorbing photothermal agents (PTAs) for antitumor therapy, antibacterial and water desalination.[6–8] More importantly, by carefully pairing electron-donating molecules and tetracyanoquinodimethane derivatives, the obtained CTCs had intense NIR-II absorption ability with high photothermal conversion efficiency, which endowed the CTCs with good phototherapeutic efficacy.[9–12] However, the assembling process and packing patterns of CTCs are complicated and hard to predict. Furthermore, the stoichiometric ratio of D and A is variable,[13] and whether eventually formed CTCs have NIR-II absorption is still contingent upon chance.[14] So it is necessary to further reveal the structure–property relationship to controllably develop CTCs with predicted performance, such as NIR-II absorption, microenvironment response, biodegradability, *etc.*

Interestingly, the CTCs often not only display newly emerging properties but also retain the inherent properties of their constituent parts.[11] Therefore, by rationally selecting D/A building blocks like pH-sensitive tetramethylbenzidine, thiol-sensitive tetracyanoquinodimethane derivatives, photosensitizer metalloporphyrin, H_2O_2-responsive metallocene, and so on, NIR-II PTT and other therapy modes including photodynamic therapy, ferrotherapy (or ferroptosis) and chemotherapy can be easily integrated into a nanoplatform for synergistic antitumor capacity to overcome intractable solid tumors.[15,16] Among them, ferroptosis, a new type of iron-dependent programmed cell death featured as the peroxidation of an unsaturated fatty acid on the cell membrane, is an ideal candidate for combination with PTT. On the one hand, ferroptosis can

[a]*Key Laboratory of Flexible Electronics (KLOFE), Institute of Advanced Materials (IAM), Nanjing Tech University (NanjingTech), 30 South Puzhu Road, Nanjing 211816, China. E-mail: iamwlsi@njtech.edu.cn; iamxcdong@njtech.edu.cn*

[b]*School of Physical Science and Information Technology, Liaocheng University, Liaocheng 252059, China*

[c]*School of Chemistry and Materials Science, Nanjing University of Information Science & Technology, Nanjing 210044, China. E-mail: ocj1987@163.com*

[d]*School of Chemistry & Materials Science, Jiangsu Normal University, Xuzhou, 221116, China*

† Electronic supplementary information (ESI) available. See https://doi.org/10.1039/d2sc03273b

© 2022 The Author(s). Published by the Royal Society of Chemistry

Open Access Article. Published on 20 July 2022. Downloaded on 4/2/2026 10:18:28 AM. This article is licensed under a Creative Commons Attribution-NonCommercial 3.0 Unported Licence.

suppress the expression of heat shock proteins (HSPs) to improve the PTT efficiency, and on the other hand, PTT can promote ferroptosis achieving a synergistic effect.[17–20] The main mechanism of ferroptosis is related to the imbalance of cellular redox homeostasis including cellular GSH depletion or ROS accumulation.[21,22] Fortunately, our group has previously observed that the CTCs containing thiol-sensitive acceptors not only possessed absorption in the NIR-II region but also showed GSH depletion induced ferroptosis, which can enhance anti-tumor efficacy.[23,24] Considering the high H_2O_2 and GSH levels in the tumor microenvironment, it is highly desired that the CTCs should simultaneously have Fenton reaction properties and GSH depletion ability so that they can effectively break redox homeostasis and promote cancer cell ferroptosis. It is well known that ferrocene derivatives have a high electron-donating ability, and display antitumor activity for catalyzing H_2O_2 to generate highly reactive ·OH,[25–27] which should be a good donor for constructing versatile CTCs. Herein, based on the crystal engineering of CTCs to enhance the ferroptosis-inducing ability and give a deep insight into the regulation mechanism for desirable NIR-II absorption, five ferrocene derivatives were chosen as donors to form corresponding complexes with F4TCNQ for their dual H_2O_2- and thiol-responsive abilities. The results indicate that the photophysical properties of CTCs are determined by the packing behaviors of F4TCNQ radical anions, and only herringbone-like packing complexes (ARSs) could realize NIR-II absorption (peak around 1060 nm) because this packing mode promotes electron delocalization along the 1D molecular chain. As expected, all NIR-II ARSs not only show a great photothermal effect (ΔT about 25 °C) under 1060 nm laser irradiation but also have biothiol (cysteine and glutathione) and H_2O_2 cascade response properties, resulting in cellular GSH depletion and ROS accumulation in tumor cells, and finally ferroptosis (Scheme 1).

Results and discussion

To explore the molecular structure–packing pattern–property relationship of CTCs, five ferrocene-based donors, including water-insoluble ferrocene (Fc) and ferrocenylmethanol (FcOH), and three water-soluble ferrocene-based quaternary ammonium salts (FcN, FcNEt, and FcNOH) were synthesized (Fig. 1a). The synthetic route is shown in Fig. S1† and the chemical structures of FcN, FcNEt, and FcNOH were confirmed by NMR (Fig. S2–S6†). 2,3,5,6-Tetrafluoro-7,7,8,8-tetracyanoquinodimethane (F4TCNQ), a strong π-acid,[23,28] was chosen as A, which could form stable anion radicals in CTCs, and the transformation diagram is shown in Fig. S7.† Then the frontier molecular orbitals of these donors were evaluated by using cyclic voltammograms (CVs) and the corresponding HOMO energy level of FcNOH, FcNEt, FcN, FcOH and Fc was calculated to be −4.52, −4.53, −4.53, −4.73 and −4.71 eV (Fig. 1b). According to previous reports, the LUMO energy level of F4TCNQ was about −5.5 eV and the large gap between the Fc-donors' HOMO and F4TCNQ's LUMO may be good for the charge transfer (Fig. 1c). Therefore, these Fc-donors were used to co-assemble with F4TCNQ to prepare the corresponding complexes (Fig. S8†). After mixing equimolar Fc-donors with F4TCNQ, all mixtures showed characteristic ESR signals centered at around 3500 gauss, demonstrating the existence of unpaired electrons (Fig. S9†). Afterward, their co-crystals were successfully prepared by solvent diffusion, and the crystal data for these CTCs are listed in Tables S1 and S2,† and the corresponding crystal structures are depicted in Fig. 1d. According to the single-crystal data, the five as-prepared Fc-based co-crystals could be divided into two groups, one having a D/A ratio of 2 : 3 ($[D_2]^{2+}[A_3]^{2-}$) and named ground CTCs (GCTCs) including Fc-F4 and FcOH-F4 co-crystals, and the other called anion-radicals salts (ARSs) with a D/A ratio of 1 : 1 ($[D]^{+}[A]^{-}$), representing FcN-F4, FcNEt-F4, and FcNOH-F4 co-crystals.

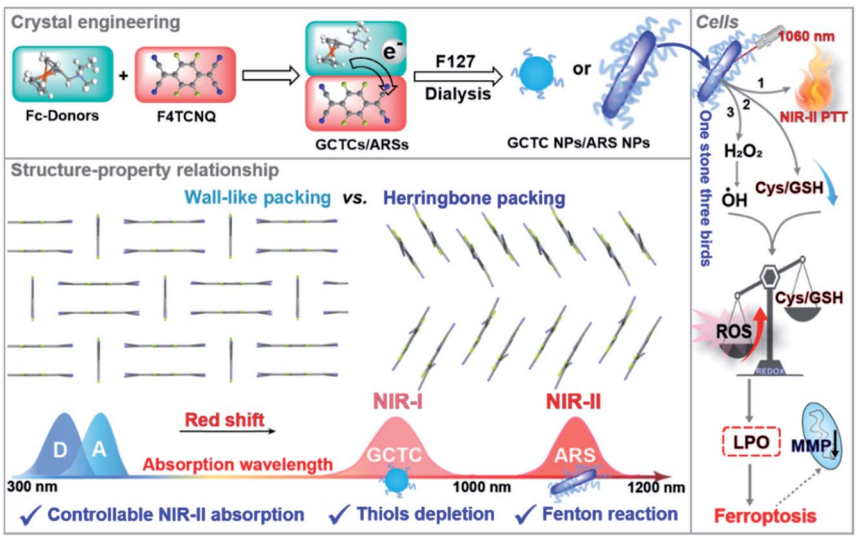

Scheme 1 Schematic illustration of the Fc-based complexes with different packing modes and photophysical properties and their antitumor mechanism.

© 2022 The Author(s). Published by the Royal Society of Chemistry

Open Access Article. Published on 20 July 2022. Downloaded on 4/2/2026 10:18:28 AM.
This article is licensed under a Creative Commons Attribution-NonCommercial 3.0 Unported Licence.

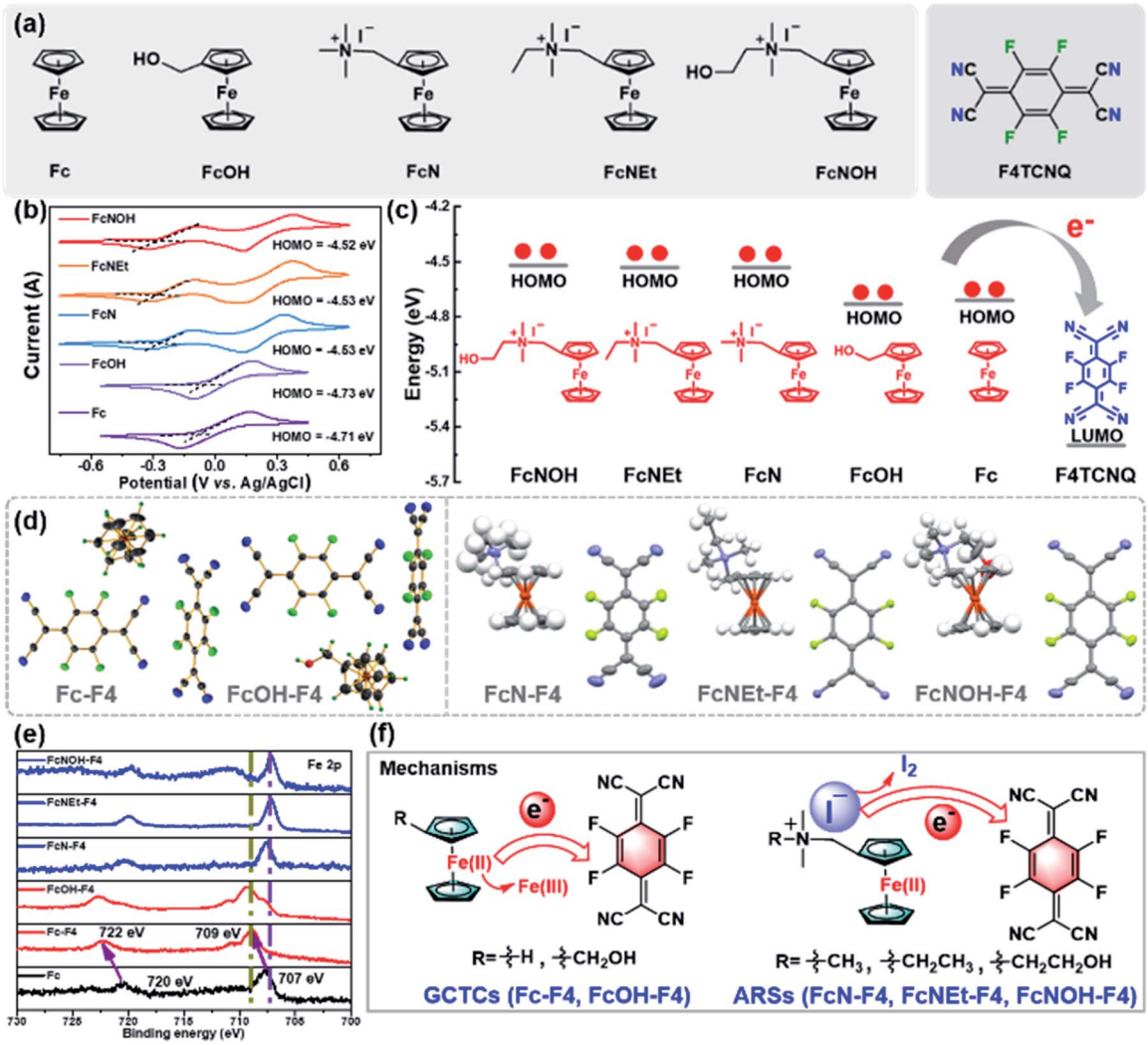

Fig. 1 (a) The chemical structures of ferrocene-based donors and F4TCNQ. (b) CVs of Fc-donors in 0.1 M *n*-$BuNPF_6$ DCM (scan rate: 50 mV s^{-1}). (c) Energy levels of Fc-donors and F4TCNQ, and schematic diagram of electron transfer from the HOMO of Fc-donors to LUMO of F4TCNQ. (d) The crystal structures of Fc-F4, FcOH-F4, FcN-F4, FcNEt-F4, and FcNOH-F4. (e) XPS spectra of Fc, Fc-F4, FcOH-F4, FcN-F4, FcNEt-F4, and FcNOH-F4. (f) Charge transfer mechanisms of GCTCs and ARSs.

In GCTCs, as shown in Fig. S10,† Fc-F4 and FcOH-F4 have similar packing behaviors and present similar bond lengths in F4TCNQ, and the C1–C2 distances in F4TCNQ are averaged around 1.41 and 1.36 Å, which are respectively referred to as the bond length of F4TCNQ radical anions and neutral F4TCNQ (about 1.37 Å, Fig. S11†). So F4TCNQ has neutral and radical anion forms in Fc-F4 and FcOH-F4, and the ratio is 1 : 2. While the three ARSs possess the same packing structures and are quite different from GCTCs, all C1–C2 bond lengths of F4TCNQ in ARSs are 1.405–1.438 Å, meaning that F4TCNQ is a radical anion and complexed with an Fc donor with 1 : 1 stoichiometry (Fig. S12 and S13†). Besides, the XPS data show that the Fe signal peaks of GCTCs appear at 709 and 722 eV which are referred to as the signals of Fe(III), while ARSs and Fc present the same Fe signal peaks at 707 and 720 eV (Fig. 1e and S14†), clearly indicating that the Fe valence state is Fe(II) in ARSs. Therefore, the charge transfer mechanism in GCTCs is that Fe(II) in the Fc core provides an electron to F4TCNQ and then turns to Fe(III) (Fig. 1f). Considering the higher reducibility of iodine ions (I^-) than that of Fe(II) (Fig. S15†), it is reasonable that iodine anions provide an electron to F4TCNQ, and then the F4TCNQ anion radical assembles with Fc-based quaternary ammonium salts to form ARSs by electrostatic Coulomb interaction (Fig. 1f).[28]

Since molecular packing behaviors are different between GCTCs and ARSs, Fc-F4 and FcNEt-F4 are chosen as model compounds to further study the packing motifs in crystals. As shown in Fig. 2a and S16,† both Fc-F4 and FcNEt-F4 adopt a lamellar and segregated packing motif, and Fc donors and F4TCNQ are located in different layers. Besides, because the unpaired electron interactions in radicals are considerably stronger than those in closed-shell compounds, it is of great importance to study the F4TCNQ radical (open-shells) packing modes. The stacks of F4TCNQ radical anions are usually not

Open Access Article. Published on 20 July 2022. Downloaded on 4/2/2026 10:18:28 AM.
This article is licensed under a Creative Commons Attribution-NonCommercial 3.0 Unported Licence.

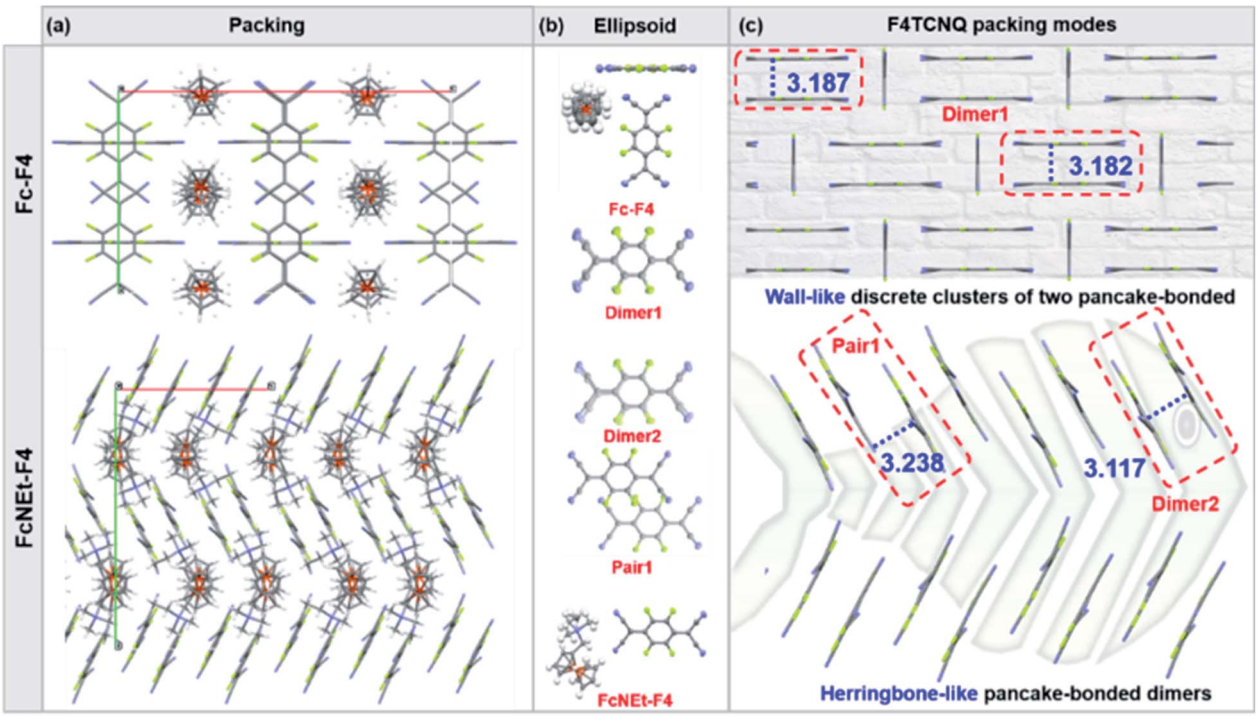

Fig. 2 (a) Packing diagrams of Fc-F4 and FcNEt-F4 co-crystal view from the c axis. (b) Ellipsoid style of Fc-F4 and FcNEt-F4 co-crystals and the vertical views of dimer 1, dimer 2 and pair 1. (c) F4TCNQ packing modes from the Fc-F4 and FcNEt-F4 co-crystals.

equidistant and have a tendency for Peierls-type distortion and pack with short π–π stacking distances (<3.2 Å), which promote dimer formation (or pancake bonds) due to the strong radical spin coupling. As shown in Fig. 2b and c, the dimers (dimer 1, dimer 2) exist in both Fc-F4 and FcNEt-F4 with a short stacking distance of 3.182(7) and 3.117 Å. But dimer 1 in Fc-F4 co-crystals is segregated by neutral F4TCNQ, which may hamper electron delocalization. In contrast, F4TCNQ anions in FcNEt-F4 first organize into radical dimers, and then the dimers align into 1D chain through π–π stacking with a distance of 3.238 Å. The results reveal that there is a strong intermolecular interaction among F4TCNQ radical anions, which promotes π-electron delocalization over the 1D chain and reduces the energy gap.

To further study the effect of different packing modes on the photophysical properties and tumor microenvironment response abilities, water-soluble Fc-based nanocomplexes were prepared *via* the re-precipitation method and their absorption spectra were recorded (Fig. 3a). As shown in Fig. S17,† Fc-based donors have no NIR absorption, with the maximum absorption peaks around 450 nm in DI water or DMSO. After self-assembling into nanoparticles, Fc-F4 and FcOH-Fc NPs (GCTC NPs) possess the characteristic absorption peaks of F4TCNQ anions and have weak absorption in the NIR-II region (Fig. 3b), while FcN-F4, FcNEt-F4 and FcNOH-F4 NPs (named ARS NPs) display a new absorption band in the NIR-II region (1000–1200 nm) with high mass extinction coefficients of 11.51, 10.15, and 9.77 L g^{-1} cm^{-1} at 1060 nm, respectively (Fig. 3c). The differences could majorly be attributed to the different packing modes in nano-complexes; the ARS NPs possess herringbone packing with short π–π distances in dimers, and the electron orbitals can delocalize along the π–π stacking direction, which can reduce the energy gap and promote the spectral red-shift. As shown in Fig. S18 and S19,† FcNEt-F4 NPs existed as 1D nanorods while Fc-F4 NPs were nanoparticles, and their XRD peaks matched well with the simulation data from the co-crystals (Fig. S20†), suggesting that Fc-F4 and FcNEt-F4 NPs kept the same packing motif as the co-crystals. In addition, the nanoparticle solutions were clarified without precipitation, indicating their good water-solubility and monodispersity (Fig. S21†). Their size distributions and zeta potentials were further tested (Fig. S22†). The zeta potentials of Fc-based nanoparticles were all negative and around −10 mV and the size of Fc-F4, FcOH-F4, FcN-F4, FcNEt-F4 and FcNOH-F4 was around 78, 88, 224, 185, and 216 nm, which were nearly consistent with the SEM/TEM images.

Inspired by outstanding NIR-II absorption ability, the photothermal effects of ARS NPs were tested under 1060 nm laser irradiation and showed power, energy and concentration dependence (Fig. S23a–c†). When the concentration is kept unchanged (c = 100 μg mL^{-1}), as the power density increased from 0.2 to 1.0 W cm^{-2} (Fig. 3d and S23d–f†), the temperature difference (ΔT) could gradually increase from 4.6 to 23.6 °C for FcNEt-F4 NPs, from 6.9 to 24.9 °C for FcN-F4 NPs, and from 6.0 to 24.2 °C for FcNOH-F4 NPs. Similarly, by changing the concentration from 0 to 100 μg mL^{-1} (P = 1.0 W cm^{-2}), the ΔT could increase from 5.4 to ~24.2 °C for ARS NPs (Fig. S23g–i† and 3e). In addition, the photothermal conversion efficiency (PCE) of FcNEt-F4 NPs was calculated to be about 53.5% (Fig. 3f and g). The results evidence that the as-prepared ARS NPs have a good NIR-II-absorption ability and photothermal effect.

© 2022 The Author(s). Published by the Royal Society of Chemistry

Open Access Article. Published on 20 July 2022. Downloaded on 4/2/2026 10:18:28 AM.
This article is licensed under a Creative Commons Attribution-NonCommercial 3.0 Unported Licence.

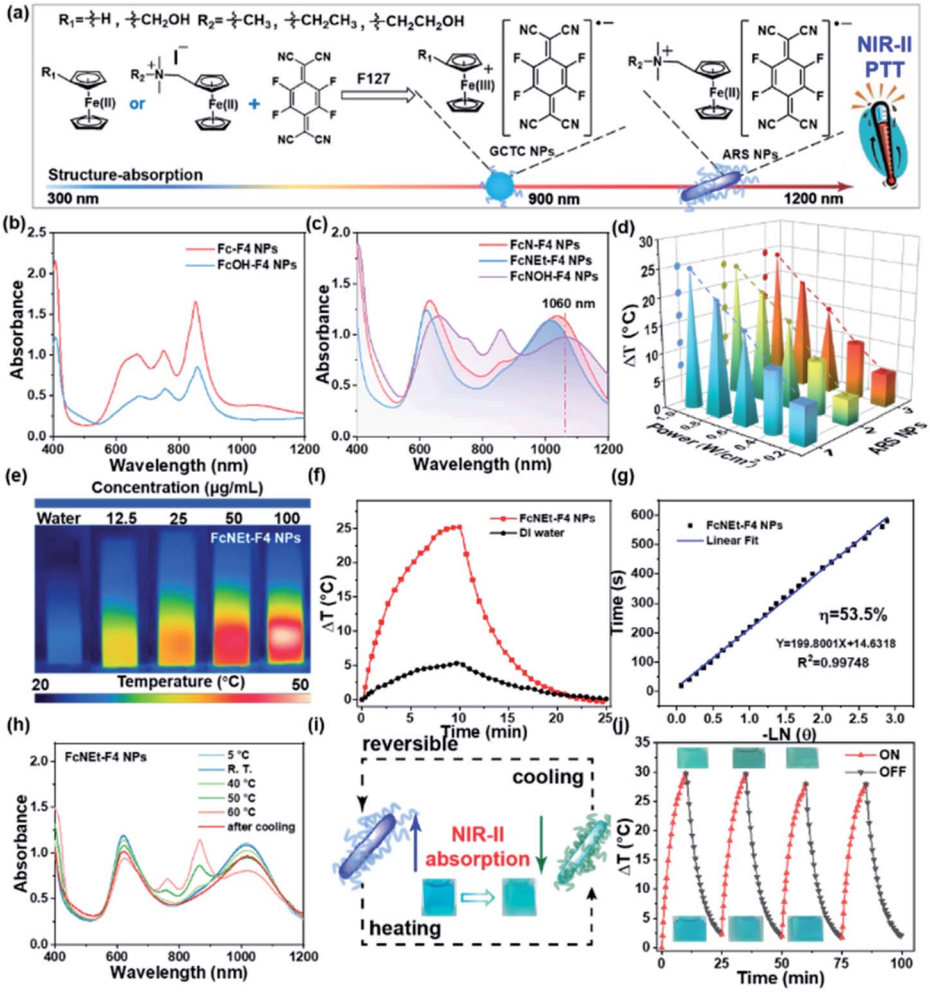

Fig. 3 (a) Preparation and property illustration of two kinds of CTC NPs. (b and c) The absorption spectra of Fc-F4, FcOH-F4, FcN-F4, FcNEt-F4, and FcNOH-F4 NPs in DI water. (d) Power density-dependent photothermal performance of ARS NPs (1–3 are FcN-F4, FcNEt-F4, and FcNOH-F4 NPs, respectively). (e) Photothermal images of different concentrations of FcNEt-F4 NPs irradiated with a 1060 nm laser ($P = 1.0$ W cm^{-2}). (f and g) Temperature rising/dropping curves of FcNEt-F4 NPs and DI water under 1060 nm laser irradiation and the plot of time *versus* $-\ln(\theta)$. (h) The absorption spectra of FcNEt-F4 NPs at different temperatures. (i) Schematic diagram of the reversible change of ARS NPs. (j) Heating and cooling cycle curves and the photographs of FcNEt-F4 NPs under on/off 1060 nm laser irradiation (1.2 W cm^{-2}).

Interestingly, ARS NPs show temperature (T) dependent absorption spectra. When the T increases from 5 to 60 °C, the absorbance around 1060 nm gradually decreases; meanwhile, a new absorption peak appears at 850 nm and the intensity gradually increases. Moreover, this newly-emerging peak would disappear and the absorption spectra of ARS NPs will partially or fully recover when the T is reduced to 5 °C (Fig. 3h and S24a–c†). These data suggest that the spectral change is a reversible process (Fig. 3i). As shown in Fig. 3j, the color of FcNEt-F4 NPs would change from blue to cyan under 1060 nm laser irradiation, while it would turn back to blue after the laser is switched off. To deeply study the reasons for the absorption change, the FcNEt-F4 co-crystal data were collected at 350 K (Table S1†). In comparison with the data collected at 150 K, FcNEt-F4 co-crystals retain the same space group and packing motif at 350 K; the big differences are the π–π stacking distances between F4TCNQ radical anions, and the distances increase from 3.117 and 3.238 Å at 150 K to 3.211 and 3.322 Å at 350 K (Fig. S25†). The larger π–π stacking distances may decrease the electron delocalization degree between the dimers and would present characteristic absorption of single dimers (F4TCNQ radical anions). The higher the temperature, the larger the distances, and the more obvious the anion absorption at 850 nm. In consideration of the T-dependent property, the stability of these ARS NPs was further investigated, and the results showed that the NPs have almost the same absorption spectra after 10 days when stored at an ambient temperature of 5 °C, while the absorbance gradually decreases at 25 °C (Fig. S26†), indicating that the F4TCNQ radical anion dimers are unstable and will decompose at high temperatures. Therefore, the as-prepared ARS NPs were stored at 5 °C for further use.

Furthermore, due to the inherent H_2O_2- and thiol-responsive abilities of Fc-cores and F4TCNQ, these ARS NPs should also possess a H_2O_2- and thiol-response, and the reactions were

Open Access Article. Published on 20 July 2022. Downloaded on 4/2/2026 10:18:28 AM.
This article is licensed under a Creative Commons Attribution-NonCommercial 3.0 Unported Licence.

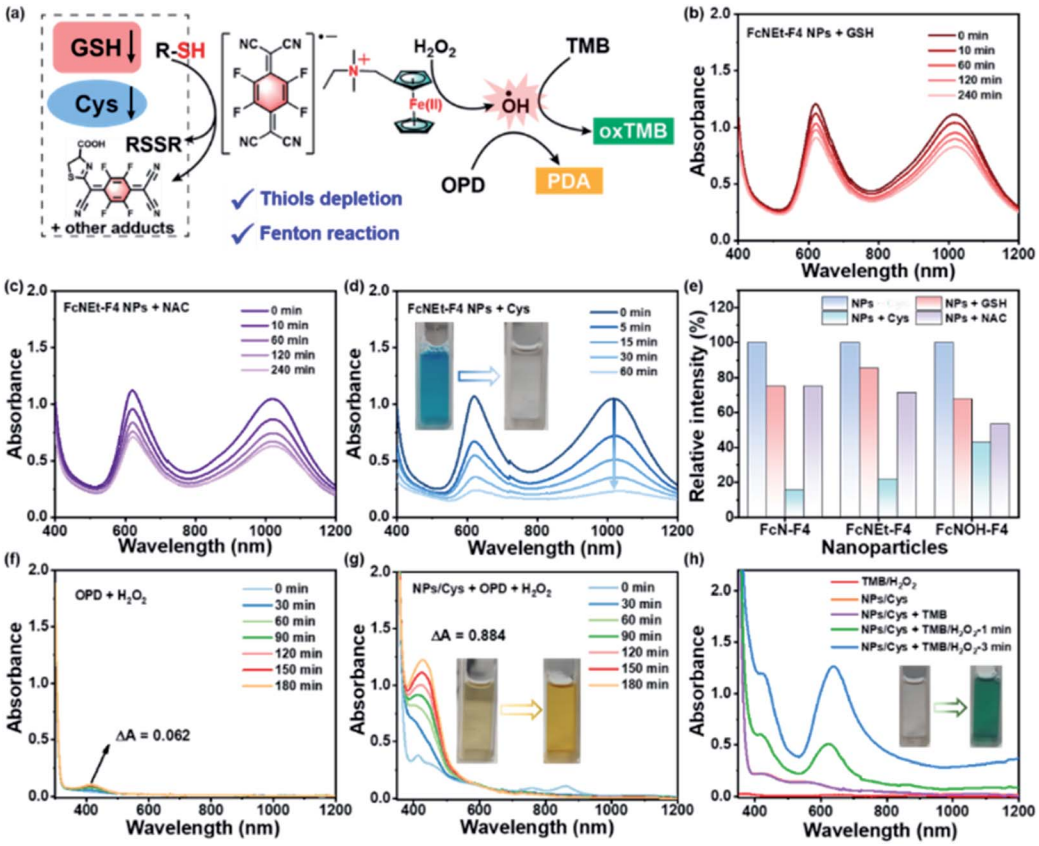

Fig. 4 (a) The mechanism of thiol depletion and ROS generation of FcNEt-F4 NPs. (b–d) The absorption spectra at different times of FcNEt-F4 NPs (100 μg mL^{-1}) incubated with GSH, NAC, and Cys solutions. (e) The degradation rate of ARS NPs after incubation with GSH, Cys, and NAC solutions. (f) The absorption spectra of OPD and H_2O_2 mixed solution. (g and h) ROS detection of Cys-incubated FcNEt-F4 NPs with OPD and TMB as probes, respectively, and photographs of the tested samples (pH = 6.0).

monitored by using a UV-vis-NIR spectrophotometer (Fig. 4a). When ARS NPs were incubated with glutathione (GSH), cysteine (Cys), and *N*-acetyl-L-cysteine (NAC), the blue color gradually faded, indicating that ARS NPs are degraded (Fig. 4b–d and S27a–i†). Among these thiols, the reactions between Cys and ARS NPs are faster than between GSH and NAC under the same conditions (Fig. 4e), and the reason should be that the cycloaddition reaction between Cys and the F4TCNQ radical anion has a faster reaction rate than the oxidation coupling of thiols. Then, we specially tested the size change of FcNEt-F4 NPs after Cys solution treatment, and after 5 minutes of co-incubation, it was obvious that small-sized nanoparticles appeared (around 10 nm), indicating that Cys reacted effectively with FcNEt-F4 NPs (Fig. S28†). However, the absorption spectra of these ARS NPs remained unchanged when other amino acids without thiols such as serine (Ser) or sarcosine (Sar) were added, suggesting that ARS NPs could specifically react with thiols (Fig. S29a–f†). In addition, after thiol incubation, the water-soluble ferrocene core could be released from NPs and serve as a catalyst for the Fenton reaction, and the Fenton reaction properties were tested with FcNEt-F4 NPs after Cys incubation (Fig. 4f–h). First, *o*-phenylenediamine (OPD) was used as the ·OH probe which could be oxidized to form phenazine-2,3-diamine (PDA). As shown in Fig. 4f and g, under weak acidic conditions (pH = 6.0), the PDA absorption difference (ΔA) was very small ($\Delta A = 0.062$) in the control group (OPD + H_2O_2), while the ΔA in the experiment group was 0.884, indicating effective ·OH generation *via* the ferrocene-catalyzed Fenton reaction. Then, 3,3′,5,5′-tetramethylbenzidine (TMB) was further used to detect ·OH production. The data in Fig. 4h show that only the experimental group (NPs/Cys + TMB/H_2O_2) possessed the oxTMB characteristic absorption peak at 650 nm, further demonstrating that the released Fc derivatives have good catalysis and ·OH generation ability. The above experimental data solidly demonstrate that the multifunctional CTCs can be easily customized *via* rationally selecting D/A building blocks according to therapeutic demand.

Considering the excellent NIR-II photothermal effect, ROS generation, and biothiol depletion abilities, the *in vitro* antitumor effect of FcNEt-F4 NPs was further investigated. As cellular essential redox substances, Cys/GSH depletion and ROS generation would break the redox homeostasis, causing intracellular reactive oxygen species (ROS) and lipid peroxide (LPO) accumulation (Fig. 5a). The cellular toxicity of FcNEt-F4 NPs for 4T1 cells was primarily evaluated *via* (4,5-dimethyl-2-thiazolyl)-2,5-diphenyl-2-*H*-tetrazolium bromide (MTT) assay, which showed concentration-dependent cell viability (Fig. 5b). FcNEt-F4 NPs have concentration-dependent dark toxicity which

© 2022 The Author(s). Published by the Royal Society of Chemistry

Open Access Article. Published on 20 July 2022. Downloaded on 4/2/2026 10:18:28 AM.
This article is licensed under a Creative Commons Attribution-NonCommercial 3.0 Unported Licence.

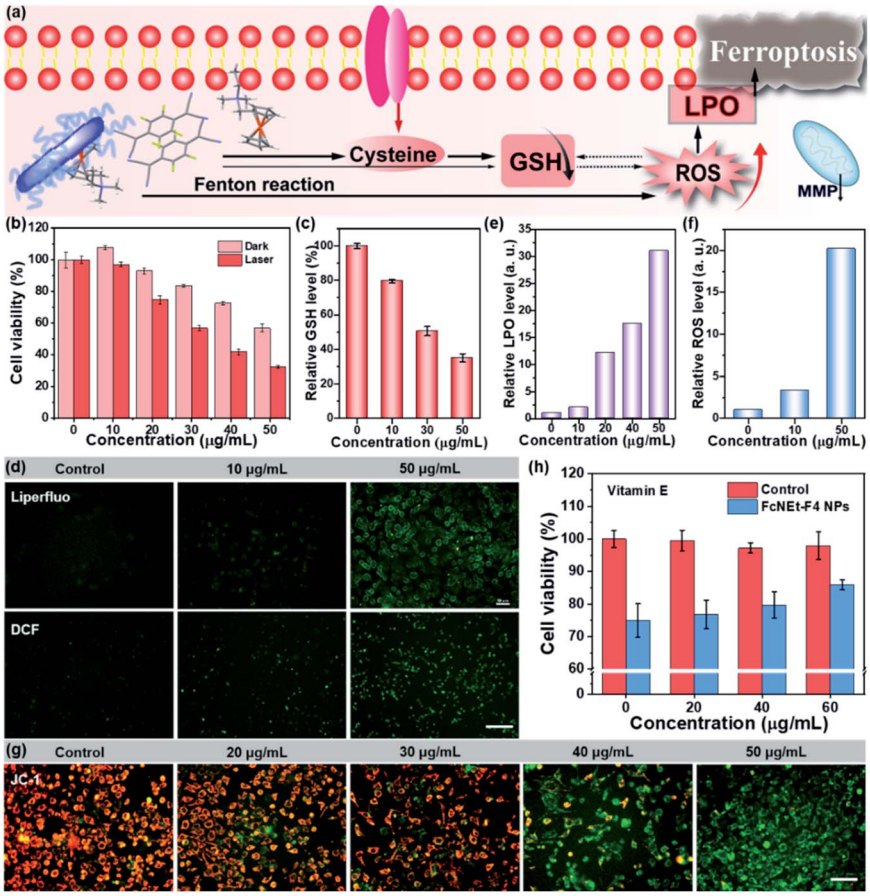

Fig. 5 (a) Schematic illustration of the ferroptosis mechanism caused by FcNEt-F4 NPs. (b) Evaluation of dark toxicity and phototoxicity of FcNEt-F4 NPs *via* MTT assay. (c) Cellular relative GSH concentrations after treating cells with different concentrations of FcNEt-F4 NPs (0, 10, 30, and 50 μg mL^{-1}). (d) The cellular LPO and ROC accumulation evaluation with Liperfluo and DCF as the green fluorescent dyes, respectively, after FcNEt-F4 NP incubation (0, 10, and 50 μg mL^{-1}). (e and f) Quantitative analysis of LPO and ROS intensity from staining images. (g) MMP analysis of staining images of 4T1 cells with JC-1 as fluorescent probes. Scale bar: 50 μm. (h) The cellular toxicity of FcNEt-F4 NPs (40 μg mL^{-1}) for 4T1 cells after adding different concentrations of vitamin E (0, 20, 40, and 60 μg mL^{-1}).

probably come from its ferroptosis-inducing ability, and the cell viability decreases to 60% after treatment with 50 μg mL^{-1} NPs. After 1060 nm laser irradiation for 5 min, FcNEt-F4 NPs show higher cytotoxicity to cancer cells, and the IC_{50} value was about 35 μg mL^{-1} due to the synergistic effect of the photothermal killing effect and ferroptosis. The live/dead cell staining images also visually confirmed the cell-killing effect of FcNEt-F4 NPs with/without laser irradiation (Fig. S30†), and both groups emitted strong green fluorescence indicating that the cells had a high survival rate, while the FcNE-F4 NP group (40 μg mL^{-1}) showed weak red fluorescence and the experimental group (40 μg mL^{-1} + laser) emitted strong red fluorescence (almost no green fluorescence), which was consistent with the MTT results. To further verify the ferroptosis-inducing ability, firstly, the intracellular GSH level was measured by using a total GSH assay kit. The results demonstrated that the GSH level was concentration-dependent when the NP concentration was increased from 10 to 50 μg mL^{-1} and the relative intracellular GSH level decreased gradually from 80% to 35%, indicating that FcNEt-F4 NPs could deplete GSH effectively (Fig. 5c). Secondly, the ROS and LPO accumulation caused by GSH depletion and the Fenton reaction was evaluated by using DCF and Liperfluo as their respective fluorescent probes (Fig. 5d). Liperfluo could be oxidized by LPO and emit green fluorescence on the membrane. As shown in Fig. 5d and S31,† the higher the concentration of FcNEt-F4 NPs, the more obvious and brighter the green fluorescence (FL) was, and there was almost no LPO FL in the control group. Fig. 5e shows a histogram of the relative LPO intensity obtained by processing staining images with MATLAB software, and it showed that the LPO level in cells treated with 50 μg mL^{-1} NPs was almost 30 times that of the control group. Similarly, the intensity of green FL from DCF is positively correlated with the cellular ROS level and it became progressively stronger as the concentration of the NPs increased from 0 to 50 μg mL^{-1} (Fig. 5d). The relative FL intensity and ROS level were obtained from images and the ROS level in the 50 μg mL^{-1} NP group was higher than in the control groups (about 20 times), while that in the 10 μg mL^{-1} NP group was 3.5 times that in the control group (Fig. 5f and S32†), suggesting that NPs could effectively deplete GSH/Cys and generate ·OH, which would break redox homeostasis and generate more ROS and LPO (Fig. 5a). Thirdly, considering that the accumulated ROS/

Open Access Article. Published on 20 July 2022. Downloaded on 4/2/2026 10:18:28 AM. This article is licensed under a Creative Commons Attribution-NonCommercial 3.0 Unported Licence.

LPO could cause mitochondrial damage reflected in the decrease of the mitochondrial membrane potential (MMP), the JC-1 probe was used to detect the MMP changes (Fig. 5g). With the concentration of FcNEt-F4 NPs increasing from 0 to 50 μg mL^{-1}, the fluorescence gradually turned from red to green which means that the MMP was gradually decreasing and finally mitochondria were dysfunctional due to ferroptosis. Besides, we further tested the cell viability under the same MTT conditions above but added vitamin E (VE), which could inhibit LPO generation as a ferroptosis inhibitor.[29] As shown in Fig. 5h, VE itself was not toxic to cells, and the cell viability of cells treated with FcNEt-F4 NPs (40 μg mL^{-1}) increased from 75% to 86% as the VE concentration increased from 0 to 60 μg mL^{-1}, showing that ferroptosis caused by FcNEt-F4 NPs was partially inhibited by VE. In addition, the LPO level in the NPs + laser (20 μg mL^{-1}) group was higher compared with that in the dark group and it became almost 1.7 times higher compared with the dark group (Fig. S29 and S33†), which led to more mitochondrial damage after laser irradiation (Fig. S34†), so the photothermal effect promotes ROS-mediated ferroptosis. The above results demonstrate that FcNEt-F4 NPs are a promising kind of NIR-II photothermal and ferroptosis-inducing agent that could effectively deplete cellular GSH and cause ROS/LPO accumulation and ferroptosis. It is expected that FcNEt-F4 and other ARS NPs could be used as novel multifunctional nano-platforms for tumor multi-modal therapies, such as PTT/ferroptosis, PTT/immunotherapy, and PTT/chemotherapy.

Conclusions

In conclusion, ferrocene and its derivatives were used as electron donors to construct various complexes with F4TCNQ. These ferrocene-based CTCs showed packing-dependent photophysical properties. And the ARS NPs, including FcN-F4, FcNEt-F4 and FcNOH-F4 NPs, present a linear dimer alignment with a short π–π stacking distance, which endows NPs with high NIR-II absorption ability and an excellent photothermal effect under 1060 nm laser irradiation. Moreover, the ARS NPs display biothiol/H_2O_2 cascade response features, which result in GSH depletion, ROS/LPO accumulation and promote ROS-mediated cell ferroptosis. *In vitro* experiments indicate that FcNEt-F4 NPs presented good cancer cell killing performance *via* the synergistic effect of NIR-II photothermal therapy and ferroptosis. This approach provides a paradigm for designing multifunctional CTCs to enhance antitumor therapeutic efficacy.

Data availability

The experimental procedures, spectra and analytical data are available in the ESI.†

Author contributions

The manuscript was written with the contributions of all authors. All authors have approved the final version of the manuscript.

Conflicts of interest

There are no conflicts to declare.

Acknowledgements

The work was supported by the NNSF of China (62120106002, 22175089, and 21975121), Jiangsu Provincial Key Research and Development Plan (BE2021711), NSF of Shandong Province (ZR2020KB018), 'Taishan Scholars' Construction Special Fund of Shandong Province, and Ningbo Science and Technology Project (202003N4048).

Notes and references

1 W. Wang, L. Luo, P. Sheng, J. Zhang and Q. Zhang, *Chemistry*, 2021, **27**, 464–490.
2 P. Hu, K. Du, F. Wei, H. Jiang and C. Kloc, *Cryst. Growth Des.*, 2016, **16**, 3019–3027.
3 D. V. Konarev, M. A. Faraonov, A. V. Kuzmin, N. G. Osipov, S. S. Khasanov, A. Otsuka, H. Yamochi, H. Kitagawa and R. N. Lyubovskaya, *New J. Chem.*, 2019, **43**, 19214–19222.
4 J. Zhang, W. Xu, P. Sheng, G. Zhao and D. Zhu, *Acc. Chem. Res.*, 2017, **50**, 1654–1662.
5 Y. Qin, J. Zhang, X. Zheng, H. Geng, G. Zhao, W. Xu, W. Hu, Z. Shuai and D. Zhu, *Adv. Mater.*, 2014, **26**, 4093–4099.
6 S. Tian, Z. Huang, J. Tan, X. Cui, Y. Xiao, Y. Wan, X. Li, Q. Zhao, S. Li and C.-S. Lee, *ACS Energy Lett.*, 2020, **5**, 2698–2705.
7 H. Xiang, Q. Yang, Y. Gao, D. Zhu, S. Pan, T. Xu and Y. Chen, *Adv. Funct. Mater.*, 2020, **30**, 1909938.
8 D. Wang, X. Kan, C. Wu, Y. Gong, G. Guo, T. Liang, L. Wang, Z. Li and Y. Zhao, *Chem. Commun.*, 2020, **56**, 5223–5226.
9 B. Tang, W. L. Li, Y. Chang, B. Yuan, Y. Wu, M. T. Zhang, J. F. Xu, J. Li and X. Zhang, *Angew. Chem., Int. Ed.*, 2019, **58**, 15526–15531.
10 S. Tian, H. Bai, S. Li, Y. Xiao, X. Cui, X. Li, J. Tan, Z. Huang, D. Shen, W. Liu, P. Wang, B. Z. Tang and C. S. Lee, *Angew. Chem., Int. Ed.*, 2021, **60**, 11758–11762.
11 W. Ge, L. Wang, J. Zhang, C. Ou, W. Si, W. Wang, Q. Zhang and X. Dong, *Adv. Mater. Interfaces*, 2020, **8**, 2001602.
12 T. Uekusa, R. Sato, D. Yoo, T. Kawamoto and T. Mori, *ACS Appl. Mater. Interfaces*, 2020, **12**, 24174–24183.
13 D. Vermeulen, L. Zhu, K. Goetz, P. Hu, H. Jiang, C. Day, O. Jurchescu, V. Coropceanu, C. Kloc and L. McNeil, *J. Phys. Chem. C*, 2014, **118**, 24688–24696.
14 L. Sun, Y. Wang, F. Yang, X. Zhang and W. Hu, *Adv. Mater.*, 2019, **31**, 1902328.
15 Y. Chen, P. He, D. Jana, D. Wang, M. Wang, P. Yu, W. Zhu and Y. Zhao, *Adv. Mater.*, 2022, **34**, 2201706.
16 Z. Wang, P. K. Upputuri, X. Zhen, R. Zhang, Y. Jiang, X. Ai, Z. Zhang, M. Hu, Z. Meng, Y. Lu, Y. Zheng, K. Pu, M. Pramanik and B. Xing, *Nano Res.*, 2018, **12**, 49–55.
17 C. Liang, X. Zhang, M. Yang and X. Dong, *Adv. Mater.*, 2019, **31**, e1904197.
18 M. Chang, Z. Hou, M. Wang, C. Yang, R. Wang, F. Li, D. Liu, T. Peng, C. Li and J. Lin, *Angew. Chem., Int. Ed.*, 2021, **60**, 12971–12979.

© 2022 The Author(s). Published by the Royal Society of Chemistry

Open Access Article. Published on 20 July 2022. Downloaded on 4/2/2026 10:18:28 AM.
This article is licensed under a Creative Commons Attribution-NonCommercial 3.0 Unported Licence.

19 C. Xue, M. Li, C. Liu, Y. Li, Y. Fei, Y. Hu, K. Cai, Y. Zhao and Z. Luo, *Angew. Chem., Int. Ed.*, 2021, **60**, 8938–8947.
20 F. Zeng, L. Tang, Q. Zhang, C. Shi, Z. Huang, S. Nijiati, X. Chen and Z. Zhou, *Angew. Chem., Int. Ed.*, 2021, e202112925.
21 C. Chen, Z. Wang, S. Jia, Y. Zhang, S. Ji, Z. Zhao, R. T. K. Kwok, J. W. Y. Lam, D. Ding, Y. Shi and B. Z. Tang, *Adv. Sci.*, 2022, e2104885.
22 T. Xu, Y. Ma, Q. Yuan, H. Hu, X. Hu, Z. Qian, J. K. Rolle, Y. Gu and S. Li, *ACS Nano*, 2020, **14**, 3414–3425.
23 C. Ou, W. Na, W. Ge, H. Huang, F. Gao, L. Zhong, Y. Zhao and X. Dong, *Angew. Chem., Int. Ed.*, 2021, **60**, 8157–8163.
24 W. Ge, Y. Xu, C. Liu, W. Xu, Y. Zhang, W. Si, W. Zhao, C. Ou and X. Dong, *J. Mater. Chem. B*, 2021, **9**, 8300–8307.
25 C. Fang, Z. Deng, G. Cao, Q. Chu, Y. Wu, X. Li, X. Peng and G. Han, *Adv. Funct. Mater.*, 2020, **30**, 1910085.
26 W. Wang, Y. Ling, Y. Zhong, Z. Li, C. Tan and Z. Mao, *Angew. Chem., Int. Ed.*, 2022, e202115247.
27 X. Fan, M. Xu, E. L. Leung, C. Jun, Z. Yuan and L. Liu, *Nano-Micro Lett.*, 2020, **12**, 76.
28 L. R. Melby, R. J. Harder, W. R. Hertler, W. Mahler, R. E. Benson and W. E. Mochel, *J. Am. Chem. Soc.*, 1962, **84**, 3374–3387.
29 C. Wu, Z. Liu, Z. Chen, D. Xu, L. Chen, H. Lin and J. Shi, *Sci. Adv.*, 2021, **7**, eabj8833.

© 2022 The Author(s). Published by the Royal Society of Chemistry